Acta Materialia 159 (2018) 123–134

Contents lists available at ScienceDirect

Acta Materialia

journal homepage: www.elsevier.com/locate/actamat

Full length article

Structures and transitions in bcc tungsten grain boundaries and their role in the absorption of point defects

Timofey Frolov [a, *], Qiang Zhu [b], Tomas Oppelstrup [a], Jaime Marian [c], Robert E. Rudd [a]

[a] Lawrence Livermore National Laboratory, Livermore, CA, 94550, USA
[b] Department of Physics and Astronomy, High Pressure Science and Engineering Center, University of Nevada, Las Vegas, NV, 89154, USA
[c] Department of Materials Science and Engineering, University of California Los Angeles, Los Angeles, CA, 90095, USA

ARTICLE INFO

Article history:
Received 2 April 2018
Received in revised form
18 June 2018
Accepted 20 July 2018
Available online 14 August 2018

Keywords:
Grain boundary
Atomistic simulations
Phase transitions
Structure prediction

ABSTRACT

We use atomistic simulations to investigate grain boundary (GB) phase transitions in elemental body-centered cubic (bcc) metal tungsten. Motivated by recent modeling study of grain boundary phase transitions in [100] symmetric tilt boundaries in face-centered cubic (fcc) copper, we perform a systematic investigation of [100] and [110] symmetric tilt high-angle and low-angle boundaries in bcc tungsten. The structures of these boundaries have been investigated previously by atomistic simulations in several different bcc metals including tungsten using the γ-surface method, which has limitations. In this work we use a recently developed computational tool based on the USPEX structure prediction code to perform an evolutionary grand canonical search of GB structure at 0 K. For high-angle [100] tilt boundaries the ground states generated by the evolutionary algorithm agree with the predictions of the γ-surface method. For the [110] tilt boundaries, the search predicts novel high-density low-energy grain boundary structures and multiple grain boundary phases within the entire misorientation range. Molecular dynamics simulation demonstrate that the new structures are more stable at high temperature. We observe first-order grain boundary phase transitions and investigate how the structural multiplicity affects the mechanisms of the point defect absorption. Specifically, we demonstrate a two-step nucleation process, when initially the point defects are absorbed through a formation of a metastable GB structure with higher density, followed by a transformation of this structure into a GB interstitial loop or a different GB phase.

1. Introduction

Grain boundaries (GBs) greatly influence many properties of engineering materials [1]. Materials with high volume fraction of GBs such as nano-crystalline and ultra-fine grain materials promise improved strength [2,3] and higher radiation tolerance [4–7]. As such they are potential candidates for materials that can operate in extreme conditions. Many energy related applications place unique demands on materials. For example in fusion, first-wall materials must withstand the thermal load and the radiation field while maintaining structural integrity both in terms of mechanical properties and in terms of resisting erosion into the plasma due to plasma-materials interaction. Tungsten has been identified as the divertor material in ITER [8] and is a leading candidate for the plasma-facing components in DEMO [9] and subsequent magnetic fusion energy systems. It has a number of advantageous properties: high thermal conductivity, acceptable activation levels, high melting temperature, mechanical strength at elevated temperatures, and resistance to surface sputtering. The questions of recrystallization and embrittlement are particularly important [10]. Plasma facing components must operate below their recrystallization temperature and they need to be replaced before undergoing brittle failure. Tungsten is known to be susceptible to embrittlement. Below its ductile-brittle transition temperature (~500 °C), pristine tungsten undergoes fracture by cleavage with essentially no plasticity prior to failure. At higher temperatures, recrystallization takes place, and GB embrittlement is the dominant fracture mode. Radiation damage affects tungsten's failure properties. Polycrystalline materials are known to have higher radiation tolerance due to presence of grain boundaries that act as sinks and sources of defects. Interaction between interfaces and point defects have been extensively investigated by both experiments and

* Corresponding author.
E-mail address: frolov2@llnl.gov (T. Frolov).

https://doi.org/10.1016/j.actamat.2018.07.051
1359-6454/

modeling, the findings are summarized in several recent reviews [11,12]. The interaction between defects and GBs is expected to depend on GB character. For example, preferential void formations was observed near crystallographically ordered boundaries in nano-twinned copper films [13]. However, all possible mechanisms and the potential role GB transitions in defect absorption are still not well understood. Predictive modeling of recrystallization and deformation of polycrystalline W relies on the accurate description of the W GBs. The goal of this work is to use atomistic modeling to investigate the structure of bcc W GBs and potential effects of point defects and elevated temperatures.

A growing number of recent studies suggests that GBs can exist in multiple different states or phases and exhibit first-order structural transformations in which the properties such as mobility, sliding resistance and solute segregation change discontinuously [14]. Experiments have revealed a potentially important role of GB phase transitions [14,15] in abnormal grain growth in ceramics [15], activated sintering [16] and liquid metal embrittlement [17]. Experimental investigation of the potential impact of GB phase transitions on microstructure and other materials properties is currently an active area of research [14,17–22].

Theoretically, GB phase transitions were investigated using phase-field models that predicted a variety of possible transformations [15,23–26]. A thermodynamic framework describing GB phase equilibrium and an adsorption equation for GB phase junctions has been recently proposed [27]. Layering transitions associated with GB segregation were investigated using lattice gas models [28–30] and first-principles calculations [31]. Although fundamentally important, the thermodynamic analysis [26,27,32–34] and phase-field models [15,23,24,26] do not provide atomic-level details about the structures of different GB phases and the mechanisms of first-order GB phase transitions.

Atomistic computer simulations have proven to be an invaluable tool for the study of GBs [1,35–38]. In the common modeling approach, also known as the γ-surface method, a GB is constructed by joining two perfect half-crystals with different orientations while sampling the possible translations of the grains relative to each other. This methodology has been employed to predict structures and energies of GBs including those in bcc materials [39–46]. The γ-surface approach has been challenged by a number of computational studies of GBs in several different materials systems. The studies demonstrated that the constant number of atoms in the simulation cell and the periodic boundary conditions prohibit the boundary from sampling all possible configurations and atoms have to be added or removed from the GB core to achieve the lowest energy configurations. These limitations became apparent in early studies of GBs in ionic crystals [47]. For example, in simulations of [001] twist boundaries in rock-salt-structured oxides the conventional methodology generates GBs with ions of the same charge overlapping at the GB plane. Strong Coulomb repulsion between the ions makes these boundaries nearly unstable with respect to dissociation into free surfaces [48]. This prediction was in apparent contradiction with experimental observations [49]. Tasker and Duffy demonstrated that the energy of these twist boundaries in oxides can be reduced significantly if a fraction of ions is removed from the GB core [47,50,51]. They proposed several low-energy structures in which the ionic density at the boundaries was optimized manually.

In face-centered cubic (fcc) metallic systems, simulations of GBs in the grand canonical ensemble demonstrated changes in GB atomic density and predicted GB structures with lower energy [52,53]. Ordered ground states of Si twist GBs were found by optimizing the atomic density and sampling the GB structure with simulated annealing [54,55]. Genetic algorithms designed to explore a diverse population of possible structures were applied to search for low-energy structures in symmetric tilt Si GBs [56] and multicomponent ceramic GBs [57].

In fcc metals new ground states and structural phase transformations were found in GBs by performing high-temperature simulations with the boundaries connected to a source/sink of atoms. Multiple GB phases characterized by different atomic densities were found in high-angle $\Sigma5(210)[001]$ and $\Sigma5(310)[001]$ GBs in Cu, Ag, Au and Ni [58]. Specifically, the calculations predicted a new GB phase called Split Kites, which has high atomic density and complex structure with a periodic unit several times larger than that of the conventional Kite phase. The new modeling methodology demonstrated fully reversible transitions with varying the temperature and/or concentration of impurities or point defects [58–61]. Both vacancies and interstitials were loaded into the GB in separate simulations and triggered transitions between the grain boundary phases with different atomic densities. This multiplicity of GB phases and GB phase transitions was demonstrated for [001] symmetric tilt GBs spanning the entire misorientation range in the same model of Cu [62]. Continuous vacancy loading into general GBs in Cu revealed lower energy states with different atomic density [63].

In bcc metals, atomically ordered GB structures with high atomic density were observed upon cyclic loading of interstitials into the $\Sigma5(210)[001]$ boundary in Mo [64]. However, the energies of these states were much higher than the energy of the ground state, making them unlikely candidates for stable GB phases. Statistical properties and multiplicity of states have been investigated in a large number of boundaries in Al, Si and W and also demonstrated the importance of the grand canonical searches [65]. Specifically, the study demonstrated that the energy of a $\Sigma5$ twist boundary in W decreased upon varying the atomic density. New ground states and grain boundary phase transformations have been demonstrated in the $\Sigma27(552)[011]$ symmetric tilt and two $\Sigma5(001)$ twist GBs in tungsten, tantalum and molybdenum [66] using the evolutionary structure prediction method [62].

Motivated by these studies and the observation of GB phase transitions in [001] symmetric tilt boundaries in Cu [58,61,62] and the $\Sigma27(552)[011]$ symmetric tilt GB in tungsten [66], in this work we conduct a systematic study of [001] and [011] symmetric tilt boundaries in bcc tungsten. We construct the boundaries at 0 K using a recently developed evolutionary grand canonical search (EGCS) method [62] which is based on the USPEX code [67] and compare the results to the predictions of the γ-surface approach. We also perform molecular dynamics simulations to investigate the effects of high temperature and point defects on the GB structure in the context of possible first-order GB phase transitions. For completeness, the previously published structure calculations for the $\Sigma27(552)[011]$ GB will be presented together with the new results. The rest of the paper is organized as follows. We describe the methodology of 0 K GB structure calculations as well as the methodology of the high-temperature molecular dynamics simulations in Section 2. We present the results of the simulations in Section 3. Our findings are summarized and discussed in Section 4.

2. Methodology of atomistic simulations

2.1. Model systems

We have modeled tungsten GBs using two different embedded-atom method (EAM) potentials: EAM1 [68] and EAM2 [69]. While several W potentials are available in the literature, we selected these because they gave better agreement with the existing DFT calculations of GB energies [70–72].

GB structure and energy calculations were performed for two different sets of boundaries. The first set contained eighteen [001]

symmetric tilt boundaries with the misorientation angle θ ranging from 0 to $\pi/2$ radians. The second set contained fifty seven [110] symmetric tilt boundaries, with the misorientation angle ranging from 0 to π. The boundaries were obtained by rotating the upper and the lower grains around the common tilt axis by the angles $\theta/2$ and $-\theta/2$, respectively. The orientations of the reference crystals were ([100], [010], [001]) and ([110], [001], [$1\bar{1}0$]) for the [001] and the [110] sets of boundaries, respectively. The boundaries were chosen to minimize the GB area for computational efficiency, while evenly sampling the entire misorientation angle range. The boundary normal was parallel to the y direction and the tilt axis was parallel to the z direction of the simulation block. Periodic boundary conditions are applied in the direction parallel to the boundary. Periodic boundary conditions were not applied in the direction normal to the boundary plane, so that the two bulk crystals were terminated by two surfaces. GB structures and energies were calculated at 0 K using the γ-surface approach as well as by the evolutionary search [62]. All energies reported were calculated at 0 K using blocks with periodic boundary conditions along GB.

2.2. γ-surface method

In the γ-surface approach two perfect half-crystals with different orientations are shifted relative to each other by a certain translation vector and then joined together. The translation is followed by a local relaxation of atoms that minimizes the energy of the system. This procedure often yields several different metastable GB states that correspond to different translation vectors. The configuration with the lowest GB energy is assumed to be the ground state. The γ-surface approach is relatively computationally inexpensive and often predicts ground state structures [73]. However, it is known to suffer from significant limitations. First, the search is not grand canonical, which in this context means that no atoms are inserted or removed from the GB core. Second, it does very poor sampling of possible GB structures: during the energy minimization the atoms simply fall into the local energy minima from their ideal lattice positions and do not explore other configurations.

2.3. Evolutionary grand-canonical search (EGCS)

In the second approach we constructed the GBs using a recently developed evolutionary algorithm [62] based on the USPEX crystal structure prediction code [67]. USPEX has proved to be extremely powerful in different systems including bulk crystals [67], 2D crystals [74], surfaces [75], polymers [76] and clusters [77]. The GB structure search algorithm samples a wide range of different atomic structures [77,78], varies the GB atomic density by inserting and removing atoms [62,77] and explores different GB dimensions [78] to search for large-area reconstructions. In the evolutionary approach the population of different GB structures improves over up to 50 generations. The details of the algorithm can be found in Ref. [62].

The evolutionary search calculations are more computationally demanding compared to the simple γ-surface approach. As a result, we investigated only a subset of representative boundaries. Out of the [001] set we selected $\Sigma5(310)[001]$ and $\Sigma5(210)[001]$ boundaries, which are the typical high-angle high-energy boundaries with misorientation angles $\theta = 36.87^\circ$ and $\theta = 53.13^\circ$, respectively. We also selected six [110] symmetric tilt boundaries: $\Sigma33(118)[1\bar{1}0]$ ($\theta = 20.1^\circ$), $\Sigma19(116)[1\bar{1}0]$ ($\theta = 26.5^\circ$), $\Sigma3(112)[1\bar{1}0]$ ($\theta = 70.5^\circ$), $\Sigma3(111)[1\bar{1}0]$ ($\theta = 109.5^\circ$), $\Sigma3(332)[1\bar{1}0]$ ($\theta = 129.5^\circ$) and $\Sigma27(552)[1\bar{1}0]$ ($\theta = 148.4^\circ$). These boundaries sample the entire misorientation range $0 < \theta < \pi$ and have been investigated recently by DFT calculations [70–72].

2.4. High-temperature simulations

To validate the ground state structures predicted at 0 K, we performed molecular dynamics simulations at high temperatures with GBs terminated at open surfaces following the methodology introduced in Ref. [58] and described in Fig. S10. Periodic boundary conditions along the boundary and constant number of atoms in the simulation block impose an unphysical constraint on the boundary structure. Such simulations do not allow for possible structural transformations of the boundary that involve changes in the number of atoms. Open surfaces provide a source and sink for atoms and effectively introduce grand canonical environment in the GB region. When the temperature is sufficiently high, GB atoms can diffuse to or from the surface and make such transformations possible. A comparison between GB structures modeled with and without periodic boundary conditions was given in our previous study [58]. The simulations were performed in the temperature range from 1000 K to 3000 K. Typical dimensions of the simulation blocks were $25.0 \times 20 \times 6$ nm^3. In the x direction the bicrystals were terminated by two open surfaces. Periodic boundary conditions were applied only along the z direction which is parallel to the tilt axis. In the direction normal the boundary plane the simulation block was terminated by two boundary regions that were kept fixed during the simulation. We also performed simulations with the bottom boundary layer fixed and the upper boundary layer floating at a rigid body as described in Fig. S10 to make sure that the boundary conditions do not affect the GB structure far away from the surfaces. We used the GB structures generated by both the γ-surface method and the evolutionary search as the initial configurations for the molecular dynamics simulations to ensure that the final GB state is independent of the initial conditions. The simulations were performed in the NVT canonical ensemble with Nose-Hoover thermostat for up to 200 ns.

To investigate how changes in the GB atomic density affect GB structure at finite temperature and demonstrate the mechanisms of point defect-GB interaction, we performed isothermal simulations with the $\Sigma5(310)[001]$ and the $\Sigma27(552)[0\bar{1}1]$ GBs using periodic boundary conditions along the boundary plane. In these simulations the interstitial atoms were injected in the bulk crystal 5 to 10 Å above the GB plane. The simulations were performed at temperatures of 2000 K and 2500 K for several tens of nanoseconds.

In the case of the $\Sigma27(552)[0\bar{1}1]$ boundary we simulated coexistence of two different GB phases in a closed system at 1500 K, 1800 K, 2000 K and 2500 K for up to 200 ns For the coexistence simulations we use a larger block with dimensions $49.5 \times 2.7 \times 13.0$ nm^3. The heterogeneous two GB state was obtained again by injecting interstitials into a half of the simulation block.

3. Results

3.1. GB structures and energies from the γ-surface approach

3.1.1. [001] symmetric tilt boundaries

Fig. 1a illustrates GB energy of the [001] symmetric tilt boundaries as a function of the misorientation angle θ generated using the γ-surface approach with the EAM1 and EAM2 potentials. The two energy cusps at $\theta = 36.87^\circ$ and $\theta = 53.13^\circ$ correspond to the $\Sigma5(310)[001]$ and $\Sigma5(210)[001]$ boundaries, respectively. The structures of these boundaries, illustrated in Supplementary Figs. S1(a and b), are well known and are composed of kite-shaped structural units. The left-hand side panel shows GB structure with the tilt axis normal to plane of the figure, while in the

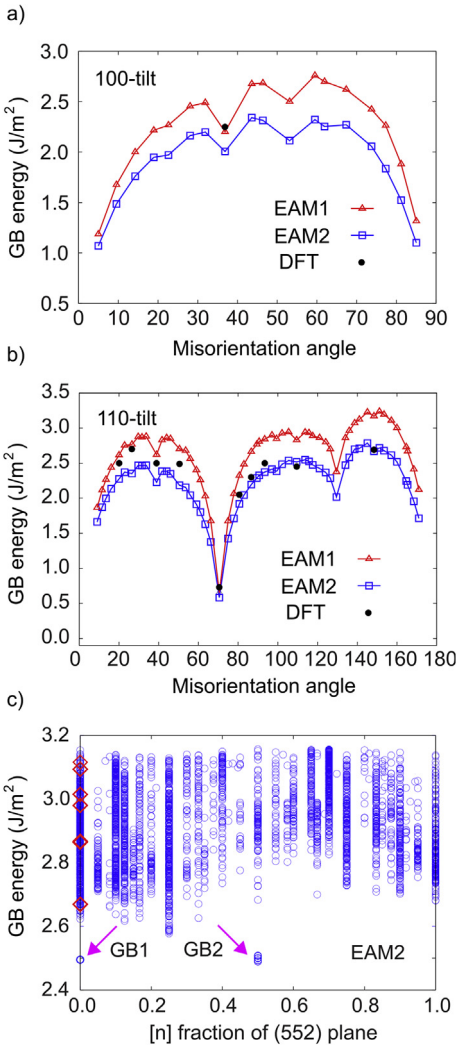

Fig. 1. a) and b) GB energy as a function of the misorientation angle θ predicted by the EAM1 and EAM2 potentials for the [100] and [110] symmetric tilt boundaries using the γ-surface method. The DFT calculated energies are taken from Ref. [71]. c) The evolutionary grand canonical search for the $\Sigma27(552)[1\bar{1}0]$ ($\theta = 148.1^\circ$) GB modeled with the EAM2 potential. GB energy of different structures generated by the algorithm (blue circles) is plotted as a function of the atomic density [n] measured as a fraction of atoms in a (552) bulk atomic plane. The search finds two low-energy GB phases at [n] = 0 and [n] = 0.5. Red diamonds illustrate the GB structures generated using the γ-surface approach. Because no atoms are inserted or removed in this approach, all red diamonds are located at $[n] = 0$. Even without changing the GB atomic density, the evolutionary search finds low-energy boundaries missed by the common methodology. (For interpretation of the references to color in this figure legend, the reader is referred to the Web version of this article.)

right-hand side panel the tilt axis is parallel to the plane of the figure. Both potentials predict similar shape of the energy curve, but the magnitude of the GB energy is somewhat different for the two potentials. The EAM1 potential due to Marinica et al. [68] shows an excellent agreement with the DFT calculations of $\Sigma5(210)[001]$ boundary from Refs. [70–72].

3.1.2. [110] symmetric tilt boundaries

Fig. 1b illustrates GB energy as a function of the misorientation angle θ calculated for the [110] symmetric tilt boundaries using the γ-surface approach with the EAM1 and EAM2 potentials. The energies of a large set of [110] symmetric tilt boundaries, generated using the same methodology, were previously calculated for bcc W, Mo and Fe using DFT calculations [70,71]. The W data points from this study are included in Fig. 1b for comparison. It is evident from the figure that the two different potentials predict similar trends in the GB energy as a function of the angle θ, but the magnitude of the energy is different. Both potentials agree reasonably well with the DFT data [70,71]. The GB energy curve has two deep cusps at $\theta = 70.5^\circ$ and $\theta = 129.5^\circ$. The deepest energy cusp at $\theta = 70.5^\circ$ corresponds to the $\Sigma3(112)[1\bar{1}0]$ boundary. The structure of this boundary is illustrated in Supplementary Fig. S1c.

Despite the similarity in the functional form of the energy curves predicted by the two potentials using the γ-surface approach, in some cases, the potentials predicted very different GB structures for the same misorientation angle. For example, Fig. 3 (a and b) illustrates two different structures of the $\Sigma33(118)[1\bar{1}0]$ (20.1°) boundary predicted by EAM1 and EAM2 potentials, respectively. The left-hand side, the middle and the right-hand side panels of the figure show three different views of the GB structure. The EAM1 structure agrees with the DFT calculations from Ref. [71]. While empirical potentials are not perfect and may predict different defect structures, below we demonstrate that the discrepancy in the predicted structure of the $\Sigma33(118)[1\bar{1}0]$ GB is due to the limitations of the γ-surface method.

3.2. Evolutionary search

We performed the evolutionary grand canonical structure search for a subset of eight GBs which included two [001] tilt boundaries and six [110] tilt boundaries. During the search the algorithm explores different atomic densities of the GB core by inserting and removing atoms. As a result, for each boundary the energy of different structures can be plotted as a function of the number of inserted atoms. Fig. 1c illustrates the results of the EGCS for the $\Sigma27(552)[1\bar{1}0]$ boundary modeled with the EAM2 potential. Each blue circle on the plot represents a GB structure generated by the evolutionary algorithm. The energy is plotted as a function of number of atoms [n] measured as a fraction of atoms in a (552) plane. To compare the results of the evolutionary search with the predictions of the common methodology we included the data points generated by the γ-surface method, which are shown on the plot as red diamonds. Notice that all the red diamonds are located at $[n] = 0$ because the γ-surface method does not insert or remove atoms from the GB core. The different energy values correspond to the different rigid translations of the grains relative to each other.

It is clear that the evolutionary search explores a much more diverse space of GB configurations. For this particular boundary it finds two distinct low-energy structures indicated by arrows at $[n] = 0$ and $[n] = 0.5$. At $[n] = 0$ the evolutionary algorithm predicts the lowest energy $\gamma_{GB} = 2.495$ J/m^2, while the best GB structure generated by the γ-surface method has a significantly higher energy of $\gamma_{GB} = 2.67$ J/m^2. In this case, the 7% reduction in energy is achieved by simply rearranging the structure, because no atoms have been added or removed. This example clearly demonstrates the insufficiency of the γ-surface method. In addition to the rearrangement of the atoms, insertion and deletion of atoms in the GB core enables the exploration of other potentially important states such as a new ground state at [n] = 0.5 with the energy $\gamma_{GB} = 2.493$ J/m^2. The low-energy structures at [n] = 0 and [n] = 0.5 represent two different phases of the $\Sigma27(552)[1\bar{1}0]$ GB.

3.2.1. EGCS for [001] symmetric tilt boundaries

Fig. 2(a and b) illustrates the results of the evolutionary search performed for the $\Sigma5(210)[001]$ and $\Sigma5(310)[001]$ GBs, respectively. In both cases the lowest energy configurations were found at [n] = 0 and matched the ground states generated by the conventional methodology. The energy of other GB configurations increased with the increasing atomic density [n] and reached the

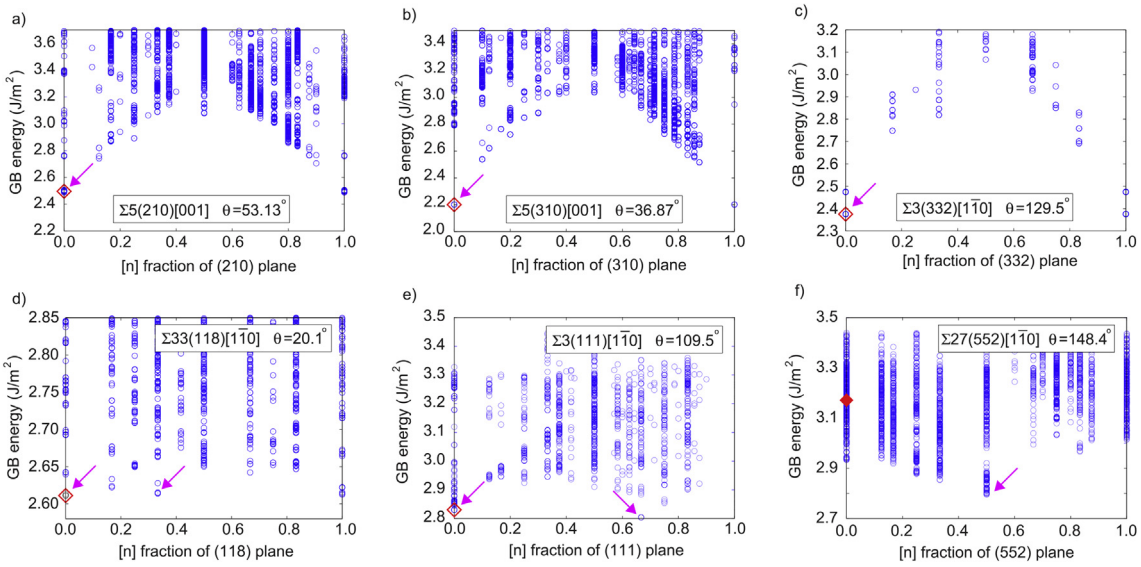

Fig. 2. Results of the evolutionary grand canonical structure search for selected [100] and [110]-tilt boundaries modeled with the EAM1 potential. GB energy is plotted as a function of the atomic density [n] measured as a fraction of atoms bulk atomic plane parallel to the boundary. In (a–c) the ground states were found at [n] = 0 and match the γ-surface structures (red diamonds). For the other three boundaries (d–f) the evolutionary search predict alternative low-energy structures with higher [n]. The different phases of these boundaries have close energies and are indicated by magenta arrows. (For interpretation of the references to color in this figure legend, the reader is referred to the Web version of this article.)

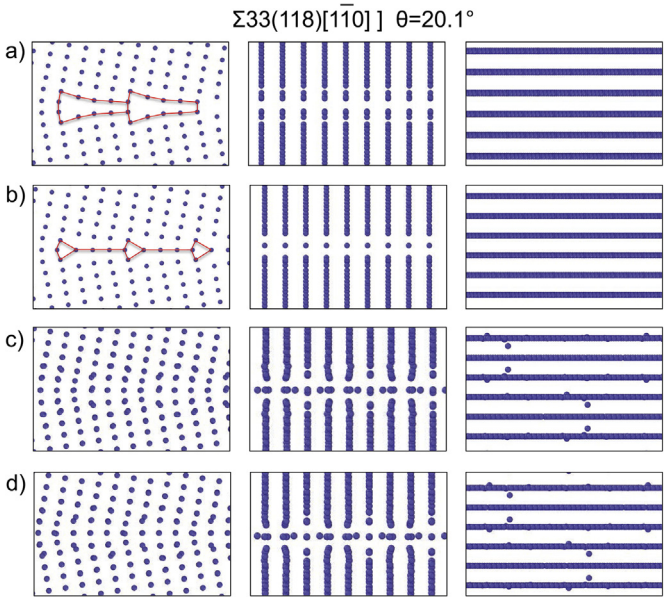

Fig. 3. Structures of the Σ33(118)[1$\bar{1}$0] ($\theta = 20.1^\circ$) GB generated by the conventional γ-surface approach and the evolutionary grand canonical search. (a) The lowest energy state generated using the γ-surface approach with the EAM1 potential with energy $\gamma_{GB} = 2.611$ J/m^2. This structure was also predicted by prior DFT calculations [70,71] that used the same methodology. (b) The lowest energy state generated using the γ-surface approach with the EAM2 potential with energy $\gamma_{GB} = 2.257$ J/m^2. (c) GB structure predicted by the evolutionary search with the EAM1 potential with the atomic fraction [n] = 1/3 and energy $\gamma_{GB} = 2.615$ J/m^2. (d) GB structure predicted by the evolutionary search using the EAM2 with the same atomic fraction [n] = 1/3 and energy $\gamma_{GB} = 2.226$ J/m^2. The left-hand, middle and right-hand panels correspond to views 1, 2 and 3 of the boundary, respectively. The different views are described in Supplementary figure S2. While the two potentials predict different GB structures at [n] = 0, new EGCS optimized states at [n] = 1/3 are the same. Views 2 and 3 reveal that in (c) and (d) the GB atoms occupy positions in between (110) planes.

highest value at $[n] = 0.5$ for the Σ5(310)[001] boundary. These results suggest that the ground states composed of kite-shaped structural units are stable against transformation to structures with other densities. The well-known ground state structures of these boundaries are illustrated in Supplementary Figs. S1(a and b). In the left-hand side panels the [001] tilt axis is normal to the plane of the figure, while it is in the plane of the figure on the right-hand side. In the schematic picture of the bicrystal in Supplementary figure S2 this two views correspond to views 1 and 2, respectively. In both boundaries the atoms are confined to (001) atomic planes of the abutting crystals.

3.2.2. EGCS for [110] symmetric tilt boundaries

The evolutionary search conducted for four [110]-tilt boundaries yielded additional GB structures that were significantly different from those generated by the γ-surface approach. The studied boundaries were selected from the entire misorientation range $0^\circ < \theta < 180^\circ$ excluding the energy cusps located at 70.5° and 129.5°. Fig. 2d–f illustrates the results of the evolutionary structure search for GBs with $\theta = 20.1^\circ$, $\theta = 109.5^\circ$ and $\theta = 148.1^\circ$ using the EAM1 potential. In contrast to the searches shown in Fig. 2a–c, each of these boundaries exhibits a minimum at atomic densities other than $[n] = 0$, suggesting possible GB phases beyond those predicted by the conventional methodology.

The GB energy cusps break the misorientation range into three intervals. In the $0^\circ < \theta < 70.5^\circ$ interval (Fig. 1b) we selected the $\theta = 20.1^\circ$ and $\theta = 26.5^\circ$ boundaries. These are relatively low-angle GBs composed of periodic arrays of edge dislocations. Fig. 2d illustrates the results of the evolutionary search for the Σ33(118)[1$\bar{1}$0] boundary at $\theta = 20.1^\circ$ modeled with the EAM1 potential. The plot has two GB energy minima: one at $[n] = 0$ and the second one at [n] = 1/3. The two low-energy configurations are indicated by arrows on the plot. The search with the EAM2 potential predicted similar behavior. At $[n] = 0$ the evolutionary search yielded GB structures identical to those generated by the γ-surface approach. As discussed earlier, the EAM1 and EAM2 potentials predict different ground states for the Σ33(118)[1$\bar{1}$0] boundary, which are illustrated in Fig. 3(a and b). The energies of these states were $\gamma_{GB} = 2.611$ J/m^2 and $\gamma_{GB} = 2.257$ J/m^2 for the EAM1 and EAM2 potentials, respectively.

On the other hand, at $[n] = 1/3$ with respect to the (118) plane, the evolutionary search predicts a new GB structure with energies $\gamma_{GB} = 2.615$ J/m^2 and $\gamma_{GB} = 2.226$ J/m^2 for EAM1 and EAM2 potentials, respectively. Thus, for each potential the energies of the $[n] = 1/3$ structure are nearly identical to those of the $[n] = 0$ structures. The $[n] = 1/3$ EGCS structures generated by EAM1 and EAM2 are illustrated in Fig. 3(c and d). Remarkably, both potentials predict the same structure. The $[n] = 1/3$ configuration is a 1×3 reconstruction, which means it has a larger unit cell compared to the γ-surface constructed boundaries. The three different views of the GB structure reveal that the extra atoms occupy interstitial positions within the GB plane. This structural feature is very different from the conventional $[n] = 0$ boundaries in which all atoms are confined to the (110) planes, as can be seen in the middle and right-hand panels of Fig. 3(a and b). Similar structures with higher atomic density [n] were predicted by the evolutionary search for the $\Sigma19(116)[1\bar{1}0]$ GB at $\theta = 26.5^\circ$.

Fig. 2e illustrates the results of the evolutionary search with the EAM1 potential for the $\Sigma3(111)[1\bar{1}0]$ at $\theta = 109.5^\circ$, which was selected as a representative high-energy boundary from the $70.5^\circ < \theta < 129.5^\circ$ interval. The energy plot again exhibits two distinct minima at $[n] = 0$ and $[n] = 2/3$ as indicated by the arrows on the plot, with the energies $\gamma_{GB} = 2.83$ J/m^2 and $\gamma_{GB} = 2.80$ J/m^2, respectively. The [n] = 2/3 is the ground state at 0 K, but the energy difference between the two structures is only 1%. Fig. 4(a and b) shows the $[n] = 0$ and $[n] = 2/3$ structures of the boundary, respectively. The $[n] = 0$ structure also generated by the γ-surface approach can be described as composed of kite-shaped structural units. The middle and right-hand panels of Fig. 4a reveal that the atoms within the boundary are confined to the misoriented $(1\bar{1}0)$ planes of the two abutting grains. The [n] = 2/3 phase is a 1×3 reconstruction, which means that the dimension of its smallest periodic unit along the $[1\bar{1}0]$ tilt axis is three times larger than that of the [n] = 0 GB phase. The middle and the right-hand panels of Fig. 4b demonstrate that the atoms of the [n] = 2/3 GB phase occupy sites between the misoriented $(1\bar{1}0)$ planes, forming an ordered structure within the GB plane.

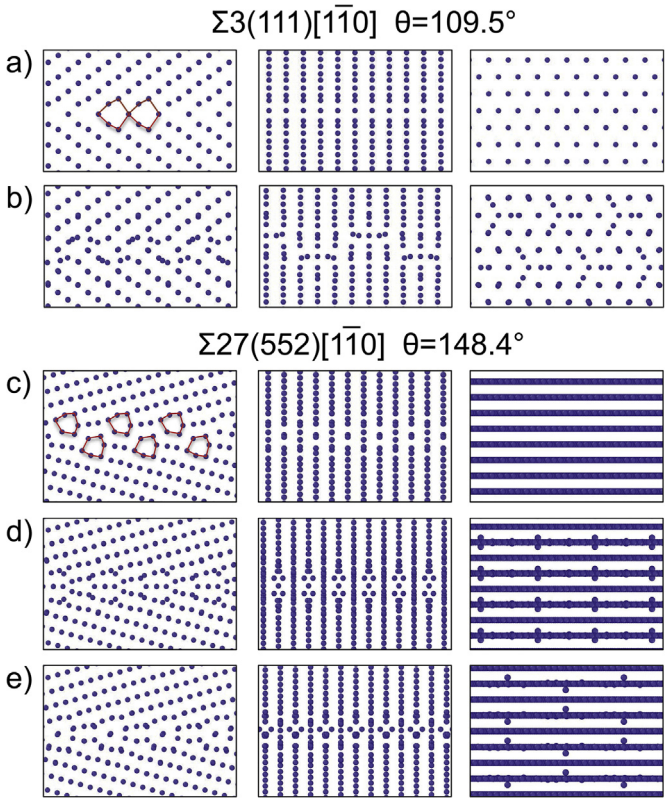

Fig. 4. Two structures of the $\Sigma3(111)[1\bar{1}0]$ ($\theta = 109.5^\circ$) GB modeled with the EAM1 potential. (a) The structure predicted by both the γ-surface approach and the evolutionary algorithm at [n] = 0 with energy $\gamma_{GB} = 2.83$ J/m^2. (b) The ground state predicted by the evolutionary algorithm at [n] = 2/3 with energy $\gamma_{GB} = 2.80$ J/m^2. (c–e) Multiple structures of the $\Sigma27(552)[1\bar{1}0]$ ($\theta = 148.4^\circ$) GB predicted by the EAM2 potential [66]. (c) Best configuration predicted by the conventional approach of γ-surface construction with GB energy $\gamma_{GB} = 2.67$ J/m^2. The evolutionary search predicts GB phases [n] = 0 (d) and [n] = 1/2 (e) with energies $\gamma_{GB} = 2.495$ J/m^2 and $\gamma_{GB} = 2.493$ J/m^2, respectively. The left-hand side, the middle and the right-hand panels correspond to view 1, view 2 and view 3 of the boundary, respectively. The different views are described in Supplementary figure S2. Views 2 and 3 reveal that the GB atoms occupy positions in between (110) planes.

Finally, in the angle range $129.5^\circ < \theta < 180^\circ$ we examined the $\Sigma27(552)[1\bar{1}0]$ boundary with at $\theta = 148^\circ$. Figs. 2f and 1c illustrate the searches for this boundary modeled with the EAM1 and EAM2 potentials, respectively. The predictions of the two potentials are somewhat different. Specifically, the EAM2 predicts two distinct low-energy GB phases located at $[n] = 0$ and $[n] = 0.5$, which were discussed earlier and illustrated in Fig. 4(d and e). On the other hand the EAM1 model predicts a single strong minimum at $[n] = 0.5$. The energy of this state, $\gamma_{GB} = 2.81$ J/m^2, is 11% lower than $\gamma_{GB} = 3.17$ J/m^2 of the conventional structure generated by the γ-surface approach. The $[n] = 0.5$ structures are 1×2 reconstructions. The ground states predicted by both potentials are not unique. Supplementary Figs. S3(b-d) illustrate several distinct structures of the $[n] = 0.5$ GB phase predicted using the EAM1 potential. The structure shown in Supplementary Figs. S3a was generated by the EAM2 potential. While the structures of these boundaries look nearly indistinguishable in the left-hand side panels, the middle and the right-hand panels clearly show different atomic arrangements. The main difference between the structures is the pattern of the occupied interstitial sites within the GB plane. Remarkably, all these configurations have nearly the same energy. The difference lies within the numerical accuracy of the calculations. The energy of these states was recently calculated using DFT calculations which confirmed the predictions of the empirical potentials EAM1 and EAM2 [66].

The evolutionary search performed for the $\Sigma3(112)[1\bar{1}0]$ ($\theta = 70.5^\circ$) and $\Sigma3(332)[1\bar{1}0]$ ($\theta = 129.5^\circ$) GBs that correspond to the GB energy cusps in Fig. 1b agreed with the γ-surface method and did not yield other alternative low-energy configurations. An example of the evolutionary search for the $\Sigma3(332)[1\bar{1}0]$ boundary modeled with the EAM1 potential is shown in Fig. 2c. It is qualitatively similar to the searches for the [001]-tilt boundaries with a single energy minimum located at the origin of the plot.

3.3. Molecular dynamics simulations

3.3.1. High-temperature simulations with open surfaces

Isothermal molecular dynamics simulations of the $\Sigma5(310)[001]$ tilt boundary with open surfaces confirmed that the structure calculated at 0 K was also stable at high temperature. We conclude that, the energy analysis at 0 K and the simulations at high temperature demonstrate that the γ-surface approach accurately predicts the ground state for this boundary.

Very different behavior, but consistent with the results of the evolutionary search at 0 K, was found for the [110] tilt boundaries. Fig. 5a–c illustrate the equilibrium structures of the $\Sigma33(118)[1\bar{1}0]$ ($\theta = 20.1^\circ$), $\Sigma3(111)[1\bar{1}0]$ ($\theta = 109.5^\circ$) and $\Sigma27(552)[1\bar{1}0]$ ($\theta = 148.1^\circ$) tilt GBs after 200 ns anneals at 2500 K. In all three cases the initial configurations were generated by the γ-surface approach. For all three boundaries these initial structures transformed to the new configurations during the simulation,

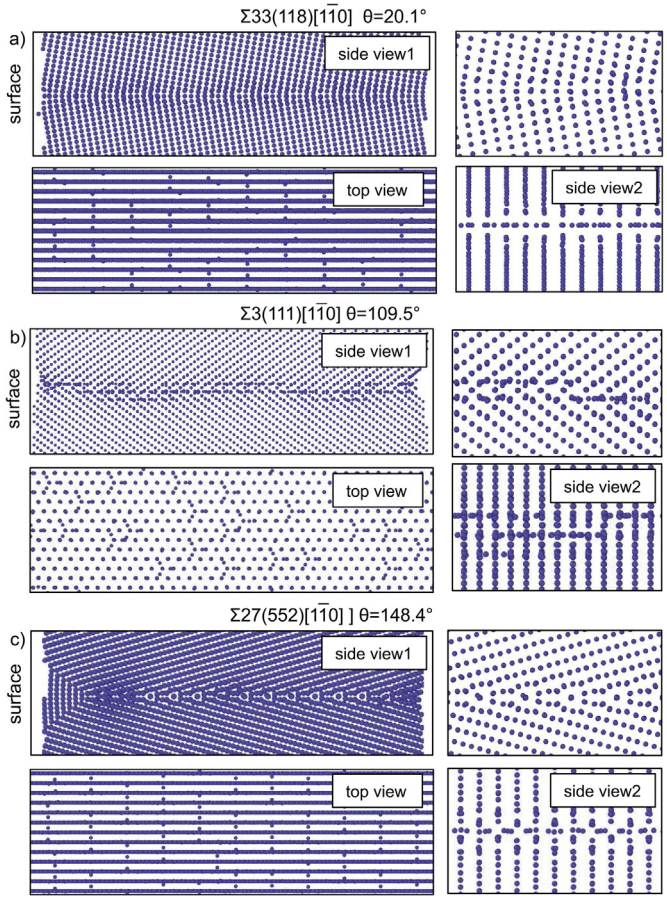

Fig. 5. Equilibrium high-temperature ordered structures of three representative [110]-tilt boundaries. The bicrystals terminated at an open surface were annealed at 2500 K for several tens of nanoseconds as shown in side view 1. Top views show the arrangement of the atoms within the boundary planes. In all three GBs the atoms can be found in-between the (110) planes. The right-hand side panels show zoomed-in views 1 and 2. The high-temperature GB structures are different from the γ-surface constructed boundaries, but matches the predictions of the EGCS calculations.

confirming the EGCS predictions. The transformations were accompanied by changes in the atomic density of GBs. The extra atoms necessary to form the new structures were supplied by GB diffusion from the open surfaces. Top views show the occupation of the interstitial sites within the GB plane. This feature of the high-temperature GB phases is common to all three boundaries and is not characteristic of the conventional structures generated by the γ-surface approach.

Fig. 5a reveals that the high-temperature structure of $\Sigma33(118)[1\bar{1}0]$ ($\theta = 20.1^\circ$) GB dislocations is more compact than that of the γ-surface GB structure. The right-hand side panels show closer views of the structure with the tilt axis normal and parallel to the plane of the figure. The interstitial columns in seeing in the top view coincide with the positions of individual dislocations. Notice that the pattern of the occupied interstitial sites varies in different dislocations, suggesting that multiple equivalent sites exist. The interstitial pattern in some regions of the boundary perfectly matches the structure generated by the evolutionary algorithm at 0 K, shown in the right-hand panel of Fig. 3(c and d).

Fig. 5b illustrates the high-temperature structure of the $\Sigma3(111)[1\bar{1}0]$ ($\theta = 109.5^\circ$) GB. The interstitial pattern (view 3) in panel b is very similar to the pattern generated by the evolutionary search at 0 K. The other views revealed the complexity of the structure. Fig. 5a illustrates what appears to be a large number of GB steps. We also performed an additional simulation with the initial structure $[n] = 2/3$ taken from the evolutionary search. The high-temperature simulation produced a structure with a different GB step pattern; however, the interstitial pattern was very similar.

Fig. 5c illustrates the bicrystal with the $\Sigma27(552)[1\bar{1}0]$ GB modeled with the EAM1 potential which was annealed at 2500 K for 100 ns The high-temperature GB structure matches the $[n] = 1/2$ GB phase obtained using the EGCS, which is illustrated in Fig. 4c–e. The interstitial pattern shown in Fig. 5c top view is similar, but does not match exactly the 0 K patterns shown in the right-hand panels of Fig. 4e and Supplementary Fig. S3. This again suggests multiple energy-equivalent sites identified at 0 K by the evolutionary search. The occupation of these sites at finite temperature is dictated by entropy. In addition to the changes in the GB structure, the surface triple junction on the left-hand side of the figure shows a chevron reconstruction. Similar reconstructions were previously observed experimentally by electron microscopy in Au [79,80]. The atoms inside the triangular region have perfect bcc structure. The two boundaries that form the chevron are the $\Sigma3(112)[1\bar{1}0]$ (70.5°) boundaries. Notice that the other surface triple junction does not undergo a similar reconstruction. Two GB units between the chevron and the rest of the [n] = 1/2 GB phase have different structures, which closely resemble the $[n] = 0$ structure generated by the EAM2 potential. While the EAM1 does not predict a low-energy configuration at this atomic fraction, it is possible that this alternative structure is stabilized by the mechanical stresses near the triple junction.

3.3.2. GB phase coexistence and point defect absorption in simulations with periodic boundary conditions

3.3.2.1. [100]-boundaries. To observe possible metastable states of the $\Sigma5(310)[001]$ boundary with higher atomic densities, we introduced interstitials into the bulk lattice just above the GB plane and annealed the blocks at 2000 K and 2500 K in separate simulations. The periodic boundary conditions were applied parallel to the boundary plane to eliminate sinks for the interstitial atoms. At both temperatures, we first observed formation of an ordered GB structure due to absorption of the interstitials. Fig. 6b illustrates the two different states of the boundary, which are similar to the structures observed by Novoselov and Yunilkin in bcc Mo [64]. This metastable configuration exists for almost 100 ns at 2000 K and several tens of nanoseconds at 2500 K before transforming into an interstitial loop at the boundary. The final state of the boundary is illustrated in Fig. 6c. The GB segment confined between the two GB dislocations is composed of perfect kite-shaped structural units. These new units appeared out of the metastable GB configuration demonstrating that the Kite structure of this boundary is very stable even at this high temperature. The relatively long lifetime of the metastable high-energy state is probably due to a large barrier of transformation that involves nucleation of the GB dislocations.

To characterize the GB disconnections we constructed closed circuits ABCF and FCDE around each of the line defects as illustrated in Fig. 6d. Summing up the lattice vectors on the reference lattice we obtain two DSC vectors with components (1/10 [310]a, 1/10 [310]a, 0) and -(1/10 [310]a, 1/10 [310]a, 0) for each disconnection. The details of the analysis are described in Supplementary Note 1 and the vectors are shown in Supplementary Figs. S4. The non-zero components of the Burgers vectors normal to the GB plane indicate that the extra materials was accommodated by an interstitial loop at the boundary. The Burgers circuit analysis used in this work is somewhat different from the analysis described in Refs. [81–83]. However, it can be shown to be equivalent for the case when the circuit cuts two identical GB segments, which is the case here.

3.3.2.2. [110]-boundaries. To test the response of the boundary

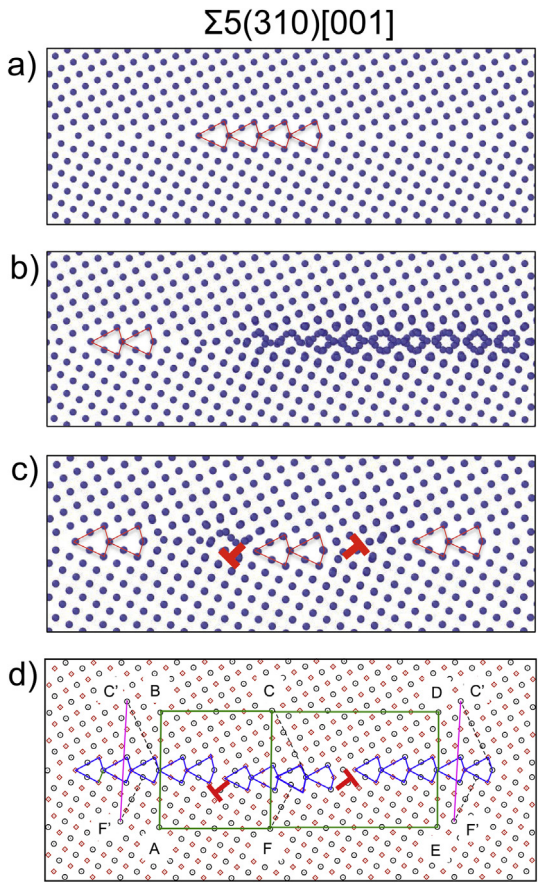

Fig. 6. (a) Interstitials are introduced into a bicrystal with a perfect Σ5(310)[001] GB. The kite-shaped structural units in the GB are outlined in red. (b) The atoms diffuse to the boundary and get absorbed by locally forming a metastable ordered GB structure with high energy. (c) At later times the metastable GB segment transforms into an interstitial loop at the GB. (d) Closed circuits ABCF and FCDE identify two disconnections $(1/10[310]a, 1/10[310]a, 0)$ and $(-1/10[310]a, 1/-10[310]a, 0)$. The Burgers vectors of each disconnection is a DCS vector equal to the sum b) AB and C'F' and c) F'C' and DE vectors, respectively. F'C' corresponds to FC vector on the reference lattice. (For interpretation of the references to color in this figure legend, the reader is referred to the Web version of this article.)

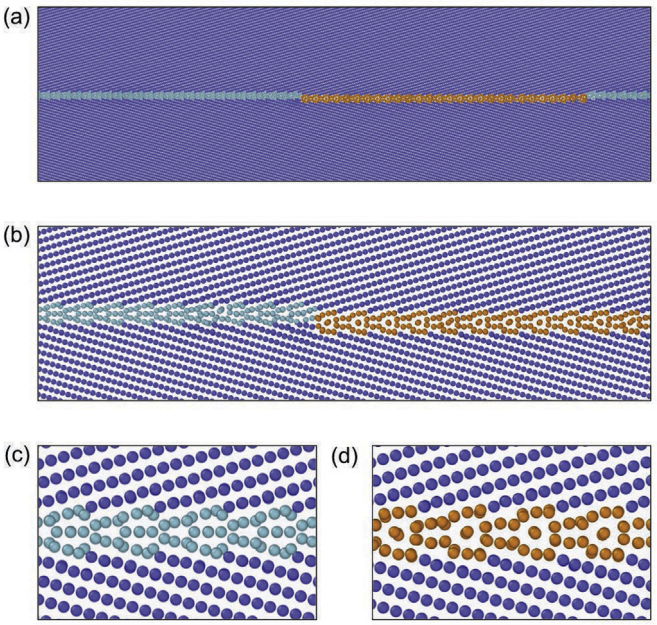

Fig. 7. (a) Equilibrium coexistence of the [n] = 0 and [n] = 1/2 GB phases of the Σ27(552)[0$\bar{1}$1] GB in a closed system with periodic boundary conditions at 1500 K. The two GB phase coexistence is implemented by introducing interstitials into perfect [n] = 0 GB phase predicted by the evolutionary search. The interstitials are absorbed when about a half of the boundary transforms into the [n] = 1/2 GB phase, also predicted by the evolutionary search. The size of each GB phase is about 25 nm in the *x* direction. (b) Two GB phases meet along a line defect that spans the periodic length of the simulation block. (c) and (d) are zoomed-in views of the two GB phases. The GB atoms are identified according to common neighbor analysis [96].

with multiple GB phases to the changes in the atomic density [n], we performed MD simulations of the Σ27(552)[110] GB with the EAM2 potential. When periodic boundary conditions are applied both GB phases [n]=0 and [n]=1/2 are stable at high temperature. The constraint of the constant number of atoms insures that one structure does not transform into another during the simulation. We used the [n]=0 structure as the initial configuration and inserted extra atoms in the bulk lattice just above the GB plane. The interstitials triggered a nucleation of the [n]=1/2 GB phase. The areal fraction of the new GB phase was dictated by the number of extra atoms introduced. Fig. 7a illustrated the structure of the boundary with two GB phases at 1500 K. The two phases are colored in orange and green in Fig. 7b. They are separated by a GB phase junction, a line defect that spans the periodic dimension normal to the plane of the figure. Fig. 7(c and d) shows zoomed in views of the two GB structures. In contrast to the Σ5(310)[001] boundary, no other transformations occurred in this simulation: the heterogeneous boundary with the two different GB phases coexisting was the final state of the simulation.

The stable equilibrium is established because the boundary is isolated from the sources and sinks of atoms. During the simulation GB atoms diffuse to establish an equilibrium concentration of vacancies or interstitials in the two different GB structures. This type of equilibrium is unique to solid systems because the solid lattice and varying number of atoms provide the system with an additional thermodynamic degree of freedom [84–86]. Indeed, according to Gibbs phase rule in an elemental system at a fixed pressure two GB phases should be able to coexist only at one temperature [27]. MD simulations of GB phase transitions in elemental systems follow this prediction when the boundary is connected to source/sink of atoms [58]. On the other hand, the GB phase coexistence in a closed system such as illustrated in Fig. 7 persists in a range of temperatures. In this work we simulated two-phase coexistence at 1500 K, 1800 K and 2000 K. The temperature changes the number of atoms [n] in each of the phases: the equilibrium concentration of vacancies and interstitials present in the coexisting GB phases. At 2500 K the [n] = 1/2 GB phase to transformed into [n] = 0. Here we label the two GB phases by referring to their atomic density at 0 K, which changes with temperature. During the transformation the extra atoms are accommodated as defects of the [n] = 0 GB phase, which apparently become energetically inexpensive at this high temperature. The solubility of defects in each GB phase became such that crossing the coexistence line became possible even in a closed system.

3.3.2.3. Nucleation and transformation of small GB islands. We find that even in the case when the different GB phases have close energies the stability of the heterogeneous GB structure may be size dependent. When a smaller number of interstitials is introduced and only a few structural units of the [n] = 1/2 boundary are formed, the small islands of the new GB phase eventually transform into the [n] = 0 structure at 2000 K as shown in Fig. 8a–c. Fig. 8(a and b) illustrate the initial homogeneous [n] = 0 GB structure and the heterogeneous GB structure after the interstitials were

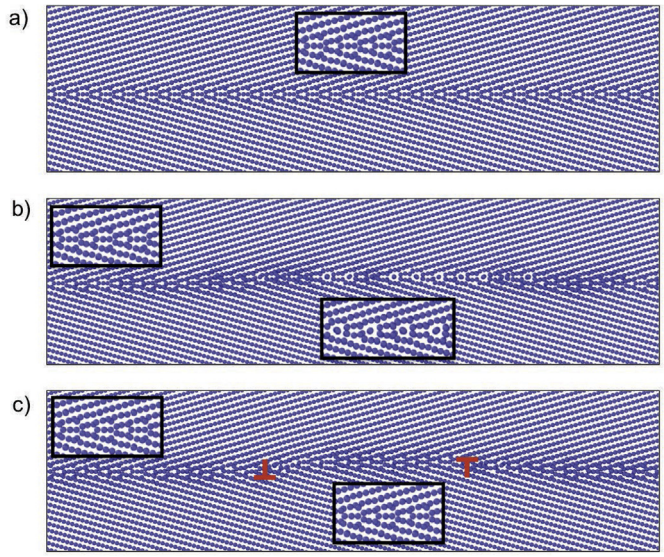

Fig. 8. (a) A smaller number of interstitials is introduced into a bicrystal with the Σ27(552)[0$\bar{1}$1] GB in an isothermal simulation at 2000 K. The initial structure corresponds to the [n] = 0 phase predicted by the evolutionary search with the EAM2 potential. After interstitial atoms are introduced in the bulk part of the upper crystal just above the GB, they quickly diffuse to the boundary core. There the interstitials are absorbed when a relatively small portion of the boundary transforms into [n] = 1/2 GB phase. The size of the [n] = 1/2 phase is about 6 nm in the *x* direction. (b) During the subsequent 50-ns-long isothermal simulation both GB phases coexist in equilibrium while exchanging atoms which diffuse along the boundary. The two different GB phases are shown in different colors. The coloring of the [n] = 1/2 structure is from a common neighbor analysis. (c) After 50 ns [n] = 1/2 phase transforms into an interstitial loop. The simulation suggests that the stability of the heterogeneous GB structure with respect to nucleation of an interstitial loop may be size dependent [96]. (For interpretation of the references to color in this figure legend, the reader is referred to the Web version of this article.)

absorbed, respectively. The mechanism is somewhat analogous to the Σ5(310)[001] boundary, in this two-step process a small island of the [n] = 1/2 phase nucleates first (Fig. 8b) and after several tens of nanoseconds it transforms into a different structure closely resembling the [n] = 0 GB phase (Fig. 8c). The defected structure is separated from the original boundary by two GB disconnections.

We analyzed the two disconnections by constructing two closed circuits around the line defects as illustrated in Supplementary Fig. S5. The CD and EF vectors cut through the transformed section of the boundary. We note that while the image of the boundary projected on the plane of the screen matches the original [n] = 0 structure, the examination of the atomic positions within the plane revealed that the transformed GB segment is significantly different and appears to have defects and even small sections of the [n] = 1/2 phase. Two similar variants with different densities [n] = 0 and [n] = 1/3 were recently demonstrated in the same Σ27 boundary in Ta [66]. It is possible, that a similar situation occurs in our tungsten simulations. Neglecting the difference between two possible variants, the vectors of the two circuits were summed following the procedure described earlier for the Σ5(310)[001] GB and identified disconnections with [1/27 [115]a/2,0,0] and [-1/27 [115]a/2,0,0] Burgers vectors. The zero component normal to the plane of the GB suggests that the extra atoms were accommodated as defects of the boundary and not as a GB dislocation loop.

4. Discussion and conclusions

In this work we studied [001] and [110] symmetric tilt GBs in bcc tungsten. These boundaries have been studied previously by atomistic simulations with empirical potentials and DFT calculations in several bcc materials including W, Mo and Fe. In these studies the GBs were generated using the common γ-surface method that performs limited sampling of GB structure and does not attempt to add or remove atoms from the GB core. In the current work, we generate the boundary structures using the new evolutionary approach [62,67]. This algorithm samples a diverse range of different structures, optimizes GB atomic density and searches for larger area reconstructions.

4.1. [001] tilt boundaries

For the [001] symmetric tilt GBs studied in this work, the γ-surface approach predicts configurations composed of kite-shaped structural units in agreement with previous studies. Our grand canonical search confirmed these structures to be the ground state for two representative high-angle high-energy GBs. Thus, contrary to [001] tilt boundaries in fcc models of Cu, Ag, Au and Ni, in bcc W the kite-shaped structural units are stable. We find alternative ordered metastable structures with higher atomic density by loading the ground state with interstitials. In these structures the extra atoms occupy interstitial positions within the GB plane located between the (001) planes of the abutting crystals. Similar structures were reported earlier in bcc Mo [64]. Our high-temperature MD simulations indicate that these denser states are stable against dissolution in the parent Kite structure even in the presence of rapid GB diffusion and survive at high temperature for relatively long time on the MD time scale. Their lifetime depends on the temperature. However, the energy of these states is still significantly higher, and at high temperature we observe a transformation into the Kite phase, which results in the formation of an interstitial loop at the GB. This transformation confirms the stability of the Kite structure even at high temperature. These modeling results are consistent with experimental observations of GB structure in other bcc metals. For example, in Mo the kite-shaped GB structure of the Σ5(310)[001] was directly observed by high-resolution transmission electron microscopy [73,87]. In Fe, a study of an asymmetric [001] boundary demonstrated faceting into Σ5(310)[001] and Σ5(210)[001] symmetric tilt boundaries with perfect Kite structures [88,89]. The atomic structure of the faceted boundary was observed by high-resolution electron microscopy and simulated with molecular dynamics. We conclude that in these [001] symmetric tilt GBs studied in elemental tungsten, the γ-surface method is likely to be sufficient to generate the GB structure at 0 K and finite temperature. The situation may be different in doped systems. A recent study of the Σ5(210)[001] Mo GB demonstrated a first-order structural transition induced by segregation of Ni [90]. Similar transitions have been demonstrated by atomistic simulations in other systems [60,91].

4.2. [110] tilt boundaries

For the majority of the [110] symmetric tilt boundaries studied in this work, which includes both high-angle and low-angle GBs, the EGCS method revealed new ground states and multiple GB phases, demonstrating that the γ-surface method is insufficient to predict the correct GB structure in these model systems. The novel GB structures cannot be described by the conventional GB structural units and they share several common features. Most of them are composed of a number of atoms incompatible with the number of atoms in the lattice planes of the abutting crystals. To obtain these structures extra atoms must be inserted into the GB core. In these structures the atoms occupy interstitial positions within the boundary plane located in between the misoriented (110) planes. The evolutionary search generated many configurations degenerate in energy, characterized by different occupation of these interstitial

positions within the boundary. The multiplicity of these states may contribute to configurational entropy and affect the stability of these structures at high temperature. It is well known that the γ-surface approach can also generate distinct GB structures with the same energy, corresponding to different grain translation vectors. For the new structures generated by the EGCS, the multiple energetically degenerate states are related by permutation of interstitial atoms without changing the grain translation vector. Finally, most of the new structures have an irreducible unit larger than the periodic units of the CSL lattice. The GB reconstructions with different dimensions often had very similar energies.

The only two [110] boundaries that did not share these properties were the $\Sigma3(112)[1\bar{1}0]$ and the $\Sigma11(332)[1\bar{1}0]$ at $\theta = 66.22^\circ$ and $\theta = 129.5^\circ$, respectively. These correspond to two energy cusps as a function of the misorientation angle. The $\Sigma3(112)[1\bar{1}0]$ has the lowest energy because of its almost bulk-like structure, so it was not surprising that the evolutionary search did not find alternative low-energy configurations. The second cusp at $\theta = 129.5^\circ$ has a noticeably higher energy, but was also identified as a stable ground state by the evolutionary search in agreement with the γ-surface method.

In some cases the new ground states generated by the EGCS algorithm had energies significantly lower than those generated by the conventional methodology, while in other cases the energies were nearly identical. For example, in the case of the $\Sigma27(552)[1\bar{1}0]$ boundary, the energy was reduced by 7–12% depending on the potential. In all boundaries with multiple distinct phases the energy difference was very small, within a few percent. While the energy reduction obtained by the advanced search was modest in some cases, the properties of different GB phases may differ significantly. For example in fcc Cu, the simulations demonstrated a strong effect of the transitions on self and impurity diffusion [58–60], segregation [60] as well as GB migration and shear strength [92]. A recent study investigated coupled motion of two [110] symmetric tilt boundaries in bcc iron and demonstrated abrupt changes in GB migration and shear stress with increasing temperature [93]. These results are consistent with multiple GB phases and GB phase transitions demonstrated in our study for the same family of symmetric tilt boundaries in a different bcc metal.

We find that overall the predictions of the two potentials EAM1 and EAM2 are consistent. Both potentials predict similar trends for the GB energy as a function of the misorientation angle. For the $\Sigma27(552)[1\bar{1}0]$ ($\theta = 148.1^\circ$) GB both potentials predict the same ground state at $[n] = 1/2$, which was confirmed by DFT calculations in our recent study [66]. EAM2 potential also predicts an additional low-energy state at $[n] = 0$. For the $\Sigma33(118)[1\bar{1}0]$ ($\theta = 20.1^\circ$) the two potentials predicted different structures within the γ-surface approach. Prior DFT calculations reported that the same GB can have these different structures in different bcc materials [71]. However, the evolutionary search for the $\Sigma33(118)[1\bar{1}0]$ boundary predicted the same ground state at $[n] = 1/3$ with both potentials. This example suggests that in some cases the discrepancy in the structure predicted by different models may be an artifact of the γ-surface approach and not the issue of the force field.

4.3. GB structures and transitions at finite temperature

The multiplicity of distinct GB structures with very close energies found at 0 K motivated further investigation of the finite-temperature GB structure. In this work we performed MD simulations at high temperature with the GBs terminated at open surfaces. The surfaces act as sources and sinks of atoms. These simulations demonstrated transformations from the $[n] = 0$ γ-surface generated structures to the structures predicted by the evolutionary with other atomic densities. Thus, despite the close energetics at 0 K, we found that the non-conventional GB structures become more stable at finite temperature. In fact, with the exception of two boundaries at $\theta = 66.22^\circ$ and $\theta = 129.5^\circ$, the structures generated by the γ-surface approach do not represent the finite-temperature structure of the [110] symmetric tilt boundaries studied.

The simulated transitions suggest that finding the lowest energy configurations and 0 K may not be sufficient to predict the structure and properties of GBs at finite temperature. In the current study the high-temperature structures were generated by the evolutionary search at 0 K and coincided with the energy minima as a function of the atomic density [n]. In general, this should not be expected. In our investigation of the [100] symmetric tilt fcc Cu boundaries we demonstrated that the high-temperature state does not correspond to GB energy minima [62], and a more sophisticated analysis is required to extract potential high-temperature structures from the results of the 0 K structure search. Specifically, we proposed a clustering procedure that groups individual structures generated by the evolutionary algorithm into GB phases. Although, we performed the grand canonical structure search for only a small subset of the boundaries, it likely that many other [110] boundaries exhibit unusual structures and multiple phases. A detailed investigation metastable structures and possible structural trends of the [110] tilt boundaries is left to future work.

High-temperature simulations with periodic boundary conditions and added point defects demonstrated nucleation of a second GB phase with different atomic density. Defect induced GB transitions have been demonstrated previously in Cu [58] and W [66]. Atomistic simulations also demonstrated that cracks and voids can be healed through a formation of a new boundary segment with a different atomic density [94]. For this simulation we selected the $\Sigma27(552)[1\bar{1}0]$ modeled with the EAM2 potential, because the boundary exhibits two different structures with the same energy at 0 K and very different atomic densities of $[n] = 0$ and $[n] = 1/2$. The simulations revealed that after the nucleation of the $[n] = 1/2$ phase, the two structures can coexist while exchanging atoms through GB diffusion. The coexistence simulations confirm that the structures represent two phases of this boundary and are not just mechanically stable configurations at 0 K. In some simulations we observed that after about 100 ns of coexistence the small secondary phase transforms into an interstitial loop at the boundary. This behavior is exactly analogous to the two-step nucleation of the interstitial loop at the $\Sigma5(310)[001]$ boundary, when the formation of a high-energy metastable GB structure induced by interstitials is followed by nucleation of GB dislocations. In the $\Sigma27(552)[1\bar{1}0]$ case, however, both GB phases have the same energy, and we speculate that the transition is driven by elastic interactions between the GB phase junctions. These line defects separate different GB phases and are likely to have dislocation character [81]. A heterogeneous boundary with a secondary phase and a homogeneous boundary with an interstitial loop represent two competing states of the boundary after it absorbs point defects. Our simulations suggest that the absorption by nucleation of a secondary GB phase is kinetically preferred, while the loop formation is more energetically favorable for some systems studied. Two-step nucleation is a well known phenomenon in bulk materials and is often observed during solidification [95]. Here we extended it to process at grain boundaries, where new interface specific factors may play an important role. For example, the stability of the heterogeneous boundaries with respect to loop nucleation or a formation of other GB phase should be influenced by elastic interactions in these systems, which are likely to be size dependent. The existing fluid-like treatments of GB phases neglect elastic effects [23,27]. The simulations motivate the development of a nucleation model that takes these elastic interactions into account.

Acknowledgment

This work was performed under the auspices of the U.S. Department of Energy (DOE) by Lawrence Livermore National Laboratory under contract DE-AC52-07NA27344. This material is based upon work supported by the U.S. DOE, Office of Science, Office of Fusion Energy Sciences. The work was supported by the Laboratory Directed Research and Development Program at LLNL, project 17-LW-012. We acknowledge the use of LC computing resources. Work in UNLV is supported by the National Nuclear Security Administration under the Stewardship Science Academic Alliances program through DOE Cooperative Agreement DE-NA0001982.

Appendix A. Supplementary data

Supplementary data related to this article can be found at https://doi.org/10.1016/j.actamat.2018.07.051.

References

[1] A.P. Sutton, R.W. Balluffi, Interfaces in Crystalline Materials, Clarendon Press, Oxford, 1995.
[2] Q. Wei, H. Zhang, B. Schuster, K. Ramesh, R. Valiev, L. Kecskes, R. Dowding, L. Magness, K. Cho, Microstructure and mechanical properties of super-strong nanocrystalline tungsten processed by high-pressure torsion, Acta Mater. 54 (2006) 4079–4089.
[3] T. Chookajorn, H.A. Murdoch, C.A. Schuh, Design of stable nanocrystalline alloys, Science 337 (2012) 951–954.
[4] O. El-Atwani, J.E. Nathaniel, A.C. Leff, K. Hattar, M.L. Taheri, Direct observation of sink-dependent defect evolution in nanocrystalline iron under irradiation, Sci. Rep. 7 (2017) 1836.
[5] O. El-Atwani, A. Suslova, T. Novakowski, K. Hattar, M. Efe, S. Harilal, A. Hassanein, In-situ TEM/heavy ion irradiation on ultrafine-and nanocrystalline-grained tungsten: effect of 3 MeV Si, Cu and W ions, Mater. Char. 99 (2015) 68–76.
[6] X.-M. Bai, A.F. Voter, R.G. Hoagland, M. Nastasi, B.P. Uberuaga, Efficient annealing of radiation damage near grain boundaries via interstitial emission, Science 327 (5973) (2010) 1631–1634.
[7] B.P. Uberuaga, L.J. Vernon, E. Martinez, A.F. Voter, The relationship between grain boundary structure, defect mobility, and grain boundary sink efficiency, Sci. Rep. 5 (2015) 9095.
[8] S. Zinkle, L. Snead, Designing radiation resistance in materials for fusion energy, Annu. Rev. Mater. Res. 44 (1) (2014) 241–267.
[9] D. Maisonnier, D. Campbell, I. Cook, L.D. Pace, L. Giancarli, J. Hayward, A.L. Puma, M. Medrano, P. Norajitra, M. Roccella, P. Sardain, M. Tran, D. Ward, Power plant conceptual studies in Europe, Nucl. Fusion 47 (11) (2007) 1524.
[10] Y. Mutoh, K. Ichikawa, K. Nagata, M. Takeuchi, Effect of rhenium addition on fracture toughness of tungsten at elevated temperatures, J. Math. Sci. 30 (1995) 770.
[11] I. Beyerlein, M. Demkowicz, A. Misra, B. Uberuaga, Defect-interface interactions, Prog. Mater. Sci. 74 (2015) 125–210.
[12] I. Beyerlein, A. Caro, M. Demkowicz, N. Mara, A. Misra, B. Uberuaga, Radiation damage tolerant nanomaterials, Mater. Today 16 (11) (2013) 443–449.
[13] T. LaGrange, K. Arakawa, H. Yasuda, M. Kumar, Preferential void formation at crystallographically ordered grain boundaries in nanotwinned copper thin films, Acta Mater. 96 (2015) 284–291.
[14] P.R. Cantwell, M. Tang, S.J. Dillon, J. Luo, G.S. Rohrer, M.P. Harmer, Grain boundary complexions, Acta Mater. 62 (2014) 1–48.
[15] S.J. Dillon, M. Tang, W.C. Carter, M.P. Harmer, Complexion: a new concept for kinetic engineering in materials science, Acta Mater. 55 (18) (2007) 6208–6218.
[16] J. Luo, H. Wang, Y.-M. Chiang, Origin of solid-state activated sintering in Bi2O3-Doped ZnO, J. Am. Ceram. Soc. 82 (4) (1999) 916–920.
[17] J. Luo, H. Cheng, K.M. Asl, C.J. Kiely, M.P. Harmer, The role of a bilayer interfacial phase on liquid metal embrittlement, Science 333 (6050) (2011) 1730–1733.
[18] M. Baram, D. Chatain, W.D. Kaplan, Nanometer-thick equilibrium films: the interface between thermodynamics and atomistics, Science 332 (6026) (2011) 206–209.
[19] M.P. Harmer, The phase behavior of interfaces, Science 332 (6026) (2011) 182–183.
[20] W. Rheinheimer, M.J. Hoffmann, Non-Arrhenius behavior of grain growth in strontium titanate: new evidence for a structural transition of grain boundaries, Scripta Mater. 101 (2015) 68–71.
[21] Z. Pan, T.J. Rupert, Formation of ordered and disordered interfacial films in immiscible metal alloys, Scripta Mater. 130 (2017) 91–95.
[22] J.D. Schuler, T.J. Rupert, Materials selection rules for amorphous complexion formation in binary metallic alloys, Acta Mater. 140 (2017) 196–205.
[23] M. Tang, W.C. Carter, R.M. Cannon, Diffuse interface model for structural transitions of grain boundaries, Phys. Rev. B 73 (2006a), 024102.
[24] M. Tang, W.C. Carter, R.M. Cannon, Grain boundary transitions in binary alloys, Phys. Rev. Lett. 97 (2006b), 075502.
[25] F. Abdeljawad, P. Lu, N. Argibay, B.G. Clark, B.L. Boyce, S.M. Foiles, Grain boundary segregation in immiscible nanocrystalline alloys, Acta Mater. 126 (2017) 528–539.
[26] Y. Mishin, W.J. Boettinger, J.A. Warren, G.B. McFadden, Thermodynamics of grain boundary premelting in alloys. I. Phase field modeling, Acta Mater (2008) submitted as Part I of this work., 2008.
[27] T. Frolov, Y. Mishin, Phases, phase equilibria, and phase rules in low-dimensional systems, J. Chem. Phys. 143 (2015), 044706.
[28] J. Rickman, H. Chan, M. Harmer, J. Luo, Grain-boundary layering transitions in a model bicrystal, Surf. Sci. 618 (2013) 88–93.
[29] J. Rickman, M. Harmer, H. Chan, Grain-boundary layering transitions and phonon engineering, Surf. Sci. 651 (2016) 1–4.
[30] J. Rickman, J. Luo, Layering transitions at grain boundaries, Curr. Opin. Solid State Mater. Sci. 20 (5) (2016) 225–230.
[31] Q. Gao, M. Widom, First-principles study of bismuth films at transition-metal grain boundaries, Phys. Rev. B 90 (2014) 144102.
[32] J.W. Cahn, Transitions and phase equilibria among grain boundary structures, J. Phys. Colloq. 43 (1982) 199–213.
[33] C. Rottman, Theory of phase transitions at internal interfaces, J. Phys. Colloq. 49 (C5) (1988) 313–322.
[34] E.W. Hart, Grain boundary phase transformations, in: H. Hu (Ed.), Nature and Behavior of Grain Boundaries, Plenum, New York, 1972, pp. 155–170.
[35] S. Ratanaphan, D.L. Olmsted, V.V. Bulatov, E.A. Holm, A.D. Rollett, G.S. Rohrer, Grain boundary energies in body-centered cubic metals, Acta Mater. 88 (2015) 346–354.
[36] K.G.F. Janssens, D. Olmsted, E.A. Holm, S.M. Foiles, S.J. Plimpton, P.M. Derlet, Computing the mobility of grain boundaries, Nat. Mater. 5 (2006) 124–127.
[37] D.L. Olmsted, S.M. Foiles, E.A. Holm, Grain Boundary Interface Roughening Transition and its Effect on Grain Boundary Mobility for Non-faceting Boundaries, vol. 57, 2007, pp. 1161–1164.
[38] D.L. Olmsted, D. Buta, A. Adland, S.M. Foiles, M. Asta, A. Karma, Dislocation-pairing transitions in hot grain boundaries, Phys. Rev. Lett. 106 (4) (2011), 046101.
[39] H.-K. Kim, W.-S. Ko, H.-J. Lee, S.G. Kim, B.-J. Lee, An identification scheme of grain boundaries and construction of a grain boundary energy database, Scripta Mater. 64 (12) (2011) 1152–1155.
[40] K. Morita, H. Nakashima, Atomic periodicity of (001) symmetric tilt boundary in molybdenum, Mater. Sci. Eng. 234 (1997) 1053–1056.
[41] M.A. Tschopp, K.N. Solanki, F. Gao, X. Sun, M.A. Khaleel, M.F. Horstemeyer, Probing grain boundary sink strength at the nanoscale: energetics and length scales of vacancy and interstitial absorption by grain boundaries in α-Fe, Phys. Rev. B 85 (2012), 064108.
[42] D. Wolf, Correlation between the energy and structure of grain boundaries in b.c.c. metals I. Symmetrical boundaries on the (110) and (100) planes, Phil. Mag. B 59 (6) (1989) 667–680.
[43] D. Wolf, Correlation between the energy and structure of grain boundaries in b.c.c. metals. II. Symmetrical tilt boundaries, Philos. Mag. A 62 (4) (1990) 447–464.
[44] D. Wolf, Structure and energy of general grain boundaries in bcc metals, J. Appl. Phys. 69 (1) (1991) 185–196.
[45] D. Yeşilleten, T.A. Arias, Atomic-level physics of grain boundaries in bcc molybdenum, Phys. Rev. B 64 (2001) 174101.
[46] E.N. Hahn, S.J. Fensin, T.C. Germann, M.A. Meyers, Symmetric tilt boundaries in body-centered cubic tantalum, Scripta Mater. 116 (2016) 108–111.
[47] P.W. Tasker, D.M. Duffy, On the structure of twist grain boundaries in ionic oxides, Philos. Mag. A 47 (6) (1983) L45–L48.
[48] D. Wolf, On the stability of (001) CSL twist boundaries in MgO : a theoretical study, J. Phys. Colloq. 43 (1982) 45–63.
[49] C.P. Sun, R.W. Balluffi, Secondary grain boundary dislocations in [001] twist boundaries in MgO I. Intrinsic structures, Philos. Mag. A 46 (1) (1982) 49–62.
[50] D.M. Duffy, P.W. Tasker, A dislocation model for the structure of [001] twist boundaries in ionic oxides, Philos. Mag. A 53 (1) (1986) 113–122.
[51] D.M. Duffy, P.W. Tasker, A general structure for coincidence twist grain boundaries in rock-salt-structured oxides, J. Am. Ceram. Soc. 67 (9) (1984) 176–177.
[52] S.R. Phillpot, J.M. Rickman, Simulated quenching to the zero-temperature limit of the grand-canonical ensemble, J. Chem. Phys. 97 (4) (1992) 2651–2658.
[53] S.R. Phillpot, Simulation of solids at nonzero temperatures in the grand-canonical ensemble, Phys. Rev. B 49 (1994) 7639–7645.
[54] S. von Alfthan, P.D. Haynes, K. Kashi, A.P. Sutton, Are the structures of twist grain boundaries in silicon ordered at 0 K? Phys. Rev. Lett. 96 (2006), 055505.
[55] S. von Alfthan, K. Kaski, A.P. Sutton, Molecular dynamics simulations of temperature-induced structural transitions at twist boundaries in silicon, Phys. Rev. B 76 (2007), 245317.
[56] J. Zhang, C.-Z. Wang, K.-M. Ho, Finding the low-energy structures of Si[001] symmetric tilted grain boundaries with a genetic algorithm, Phys. Rev. B 80 (2009), 174102.
[57] A.L.S. Chua, N.A. Benedek, L. Chen, M.W. Finnis, A.P. Sutton, A genetic algorithm for predicting the structures of interfaces in multicomponent systems,

Nat. Mater. 9 (5) (2010) 418–422.
[58] T. Frolov, D.L. Olmsted, M. Asta, Y. Mishin, Structural phase transformations in metallic grain boundaries, Nat. Commun. 4 (2013a) 1899.
[59] T. Frolov, S.V. Divinski, M. Asta, Y. Mishin, Effect of interface phase transformations on diffusion and segregation in high-angle grain boundaries, Phys. Rev. Lett. 110 (2013b) 255502.
[60] T. Frolov, M. Asta, Y. Mishin, Segregation-induced phase transformations in grain boundaries, Phys. Rev. B 92 (2015), 020103.
[61] T. Frolov, M. Asta, Y. Mishin, Phase transformations at interfaces: observations from atomistic modeling, Curr. Opin. Solid State Mater. Sci. 20 (5) (2016) 308–315.
[62] Q. Zhu, A. Samanta, B. Li, R.E. Rudd, T. Frolov, Predicting phase behavior of grain boundaries with evolutionary search and machine learning, Nat. Commun. 9 (2018) 467.
[63] W. Yu, M. Demkowicz, Non-coherent Cu grain boundaries driven by continuous vacancy loading, J. Mater. Sci. 50 (11) (2015) 4047–4065.
[64] I. Novoselov, A. Yanilkin, Impact of segregated interstitials on structures and energies of tilt grain boundaries in Mo, Comput. Mater. Sci. 112 (Part A) (2016) 276–281.
[65] J. Han, V. Vitek, D.J. Srolovitz, The grain-boundary structural unit model redux, Acta Mater. 133 (2017) 186–199.
[66] T.V. Frolov, W. Setyawan, R. Kurtz, J. Marian, A. Oganov, R.E. Rudd, Q. Zhu, Grain boundary phases in bcc metals, Nanoscale 10 (2018) 8253–8268.
[67] A.R. Oganov, C.W. Glass, Crystal structure prediction using ab initio evolutionary techniques: principles and applications, J. Chem. Phys. 124 (24) (2006), 244704.
[68] M.C. Marinica, L. Ventelon, M.R. Gilbert, L. Proville, S.L. Dudarev, J. Marian, G. Bencteux, F. Willaime, Interatomic potentials for modelling radiation defects and dislocations in tungsten, J. Phys. Condens. Matter 25 (39) (2013), 395502.
[69] X. Zhou, H. Wadley, R. Johnson, D. Larson, N. Tabat, A. Cerezo, A. Petford-Long, G. Smith, P. Clifton, R. Martens, T. Kelly, Atomic scale structure of sputtered metal multilayers, Acta Mater. 49 (19) (2001) 4005–4015.
[70] W. Setyawan, R.J. Kurtz, Ab initio study of H, He, Li and Be impurity effect in tungsten $\sum$3 (112) and $\sum$27 (552) grain boundaries, J. Phys. Condens. Matter 26 (13) (2014), 135004.
[71] D. Scheiber, R. Pippan, P. Puschnig, L. Romaner, Ab initio calculations of grain boundaries in bcc metals, Model. Simulat. Mater. Sci. Eng. 24 (3) (2016), 035013.
[72] W. Setyawan, R.J. Kurtz, Effects of transition metals on the grain boundary cohesion in tungsten, Scripta Mater. 66 (8) (2012) 558–561.
[73] G. Campbell, J. Belak, J. Moriarty, Atomic structure of the $\sum$5 (310)/[001] symmetric tilt grain boundary in molybdenum, Acta Mater. 47 (15) (1999) 3977–3985.
[74] X.-F. Zhou, X. Dong, A.R. Oganov, Q. Zhu, Y. Tian, H.-T. Wang, Semimetallic two-dimensional boron allotrope with massless Dirac fermions, Phys. Rev. Lett. 112 (2014), 085502.
[75] Q. Zhu, L. Li, A.R. Oganov, P.B. Allen, Evolutionary method for predicting surface reconstructions with variable stoichiometry, Phys. Rev. B 87 (2013), 195317.
[76] Q. Zhu, V. Sharma, A.R. Oganov, R. Ramprasad, Predicting polymeric crystal structures by evolutionary algorithms, J. Chem. Phys. 141 (15) (2014), 154102.
[77] A.O. Lyakhov, A.R. Oganov, H.T. Stokes, Q. Zhu, New developments in evolutionary structure prediction algorithm USPEX, Comput. Phys. Commun. 184 (4) (2013) 1172–1182.
[78] Q. Zhu, A.R. Oganov, A.O. Lyakhov, X. Yu, Generalized evolutionary metadynamics for sampling the energy landscapes and its applications, Phys. Rev. B 92 (2015), 024106.
[79] F. Lançon, T. Radetic, U. Dahmen, Stability of the chevron domain at triple-line reconstructions, Phys. Rev. B 69 (2004) 172102.
[80] T. Radetic, F. Lançon, U. Dahmen, Chevron defect at the intersection of grain boundaries with free surfaces in Au, Phys. Rev. Lett. 89 (2002), 085502.
[81] J.P. Hirth, R.C. Pond, Steps, dislocations and disconnections as interface defects relating to structure and phase transformations, Acta Mater. 44 (1996) 4749–4763.
[82] R.C. Pond, S. Celotto, Special interfaces: military transformations, Int. Mater. Rev. 48 (2003) 225–245.
[83] J. Hirth, R. Pond, R. Hoagland, X.-Y. Liu, J. Wang, Interface defects, reference spaces and the Frank-Bilby equation, Prog. Mater. Sci. 58 (5) (2013) 749–823.
[84] F.C. Larche, J.W. Cahn, Thermochemical equilibrium of multiphase solids under stress, Acta Metall. 26 (1978) 1579–1589.
[85] W.W. Mullins, R.F. Sekerka, On the thermodynamics of crystalline solids, J. Chem. Phys. 82 (11) (1985) 5192–5202.
[86] P. Voorhees, W.C. Johnson, The Thermodynamics of Elastically Stressed Crystals, Vol. 59 of Solid State Physics, Academic Press, 2004, 1 – 201.
[87] G.H. Campbell, M. Kumar, W.E. King, J. Belak, J.A. Moriarty, S.M. Foiles, The rigid-body displacement observed at the $\sum$= 5, (310)-[001] symmetric tilt grain boundary in central transition bcc metals, Philos. Mag. A 82 (2002) 1573–1594.
[88] D. Medlin, K. Hattar, J. Zimmerman, F. Abdeljawad, S. Foiles, Defect character at grain boundary facet junctions: analysis of an asymmetric $\sum$= 5 grain boundary in Fe, Acta Mater. 124 (2017) 383–396.
[89] F. Abdeljawad, D.L. Medlin, J.A. Zimmerman, K. Hattar, S.M. Foiles, A diffuse interface model of grain boundary faceting, J. Appl. Phys. 119 (23) (2016), 235306.
[90] S. Yang, N. Zhou, H. Zheng, S.P. Ong, J. Luo, First-order interfacial transformations with a critical point: breaking the symmetry at a symmetric tilt grain boundary, Phys. Rev. Lett. 120 (2018), 085702.
[91] C.J. O'Brien, C.M. Barr, P.M. Price, K. Hattar, S.M. Foiles, Grain boundary phase transformations in PtAu and relevance to thermal stabilization of bulk nanocrystalline metals, J. Mater. Sci. 53 (4) (2018) 2911–2927.
[92] T. Frolov, Effect of interfacial structural phase transitions on the coupled motion of grain boundaries: a molecular dynamics study, Appl. Phys. Lett. 104 (21) (2014), 211905.
[93] J. Yin, Y. Wang, X. Yan, H. Hou, J.T. Wang, Atomistic simulation of shear-coupled motion of [110] symmetric tilt grain boundary in α-iron, Comput. Mater. Sci. 148 (2018) 141–148.
[94] M. Aramfard, C. Deng, Mechanically enhanced grain boundary structural phase transformation in Cu, Acta Mater. 146 (2018) 304–313.
[95] D. Erdemir, A.Y. Lee, A.S. Myerson, Nucleation of crystals from solution: classical and two-step models, Acc. Chem. Res. 42 (5) (2009) 621–629.
[96] A. Stukowski, Visualization and analysis of atomistic simulation data with OVITO–the Open Visualization Tool, Model. Simulat. Mater. Sci. Eng. 18 (1) (2010), 015012.